

Article

Assessing Strain Rate Sensitivity of Nanotwinned Al–Zr Alloys through Nanoindentation

Nicholas Allen Richter ¹, Xuanyu Sheng ¹, Bo Yang ¹, Benjamin Thomas Stegman ¹, Haiyan Wang ^{1,2}
and Xinghang Zhang ^{1,*}

¹ School of Materials Engineering, Purdue University, West Lafayette, IN 47907, USA

² School of Electrical and Computer Engineering, Purdue University, West Lafayette, IN 47907, USA

* Correspondence: xzhang98@purdue.edu

Abstract: Nanotwinned metals have exhibited many enhanced physical and mechanical properties. Twin boundaries have recently been introduced into sputtered Al alloys in spite of their high stacking fault energy. These twinned Al alloys possess unique microstructures composed of vertically aligned $\Sigma 3(112)$ incoherent twin boundaries (ITBs) and have demonstrated remarkable mechanical strengths and thermal stability. However, their strain rate sensitivity has not been fully assessed. A modified nanoindentation method has been employed here to accurately determine the strain rate sensitivity of nanotwinned Al–Zr alloys. The hardness of these alloys reaches 4.2 GPa while simultaneously exhibiting an improved strain rate sensitivity. The nanotwinned Al–Zr alloys have shown grain size-dependent strain rate sensitivity, consistent with previous findings in the literature. This work provides insight into a previously unstudied aspect of nanotwinned Al alloys.

Keywords: nanotwinned metals; strain rate sensitivity; nanoindentation; transmission electron microscopy; aluminum alloys



Citation: Richter, N.A.; Sheng, X.; Yang, B.; Stegman, B.T.; Wang, H.; Zhang, X. Assessing Strain Rate Sensitivity of Nanotwinned Al–Zr Alloys through Nanoindentation. *Crystals* **2023**, *13*, 276. <https://doi.org/10.3390/cryst13020276>

Academic Editor: Ronald W. Armstrong

Received: 18 January 2023

Revised: 29 January 2023

Accepted: 31 January 2023

Published: 5 February 2023



Copyright: © 2023 by the authors. Licensee MDPI, Basel, Switzerland. This article is an open access article distributed under the terms and conditions of the Creative Commons Attribution (CC BY) license (<https://creativecommons.org/licenses/by/4.0/>).

1. Introduction

The mechanical strength of single-phase metallic materials is often largely determined by their grain size (d), and such dependence is often described by the classic Hall–Petch relationship [1–4]:

$$\sigma_y = \sigma_0 + k_y d^{-\frac{1}{2}} \quad (1)$$

where σ_y is the yield strength, σ_0 is the friction stress, and k_y is the Hall–Petch coefficient. Various efforts have been made to push material grain sizes into the nanometer regime [5,6] via severe plastic deformation [7–10], physical vapor deposition [11–15], and inert gas condensation [16–19]. These studies have focused on nanocrystalline (NC) materials with grain sizes of less than 100 nm that show remarkable mechanical properties as well as novel grain boundary (GB)-mediated deformation mechanisms [20]. Another mechanical property closely linked to GB spacing is strain rate sensitivity (SRS) [21]. SRS is an important parameter that describes both the deformability and thermally activated deformation (creep) of metallic materials [22–24]. Correspondingly, increasing the SRS exponent (m) is typically linked to enhanced ductility [21,22]. The variation in SRS of metallic materials is also heavily dependent on their crystal structures. Body-centered cubic (BCC) metals are much more sensitive to changes in temperature and strain rate than face-centered cubic (FCC) metals due to their lower activation volumes [21,25–27]. FCC metals exhibit increasing SRS with decreasing grain sizes, while BCC metals show the opposite trend [22,25,27]. Chen et al. demonstrated that UFG and NC FCC Cu revealed increasing m with decreasing grain size [24]. Quantifying the relationship between SRS and microstructures is crucial to fully understand the mechanical response of NC metallic materials.

Nanotwinned (NT) metals have been extensively investigated due to their simultaneous increase in strength and ductility [28–32]. Most prior studies on NT metals have

focused on systems with low stacking fault energy (SFE) [33–35], characteristic of a few FCC metals including Cu (22 mJ/m²) [36,37], Ag (16 mJ/m²) [38,39], and several stainless steels (~50 mJ/m²) [40]. A high SFE provides a significant barrier to twin formation [41]. Recently, magnetron sputtering has been used to stabilize far-from-equilibrium NT structures in high SFE Al films [42–44]. The addition of transition metal solute reduces twin spacing and can further promote the strong {111} texture needed to form vertically aligned Σ 3(112) incoherent twin boundaries (ITBs) [45–51]. Zhang et al. reported a flow strength of ~2 GPa in NT Al–Ni alloys using in situ micropillar compression while maintaining remarkable deformability and thermal stability [52,53]. Molecular dynamics (MD) simulations and in situ mechanical testing identified the mobility of the partial dislocations composing the 9R phase as a significant factor in accommodating the deformability of NT Al alloys while simultaneously providing a barrier to dislocation motion [48]. Zr solute has proven effective in promoting a high twin density and large volume fraction in the 9R phase [45,46]. Additionally, Zr enables prominent thermal stability of nanostructures in NT Al–Co–Zr alloys [44]. Understanding the behavior of Zr solute in Al is also relevant to a range of cast and additively manufactured Al alloys [54–56]. NT metals have also exhibited enhanced SRS due to the activation of Shockley partial dislocations [57,58]. However, the contribution of ITBs on the SRS of NT Al alloys has not been explored to date and remains a gap in current understanding.

In this study, we applied a nanoindentation technique to probe the SRS of NT Al–Zr. We used the modified nanoindentation technique to overcome the difficulty of large measurement uncertainty at a low strain rate and were able to arrive at a reliable SRS for specimens. The NT Al alloys exhibit grain size-dependent SRS comparable to Al and Al alloys with similar grain sizes. The roles of ITB microstructure and partial dislocations on enhanced SRS in NT Al alloys are discussed.

2. Materials and Methods

Several 2 μ m Al–Zr alloy films with 50 nm Ag seed layers were magnetron sputtered at room temperature onto HF-etched Si(111) substrates. The Ag seed layer serves to promote a strong (111) texture in the Al–Zr alloy films due to the similarity in lattice parameters. Targets of 99.999% Al, 99.995% Zr, and 99.999% Ag were used for deposition at a gas pressure of 3.5 mTorr. The chamber base pressure was evacuated to 5×10^{-9} Torr. A Panalytical Empyrean X'pert PRO MRD diffractometer was used to collect out-of-plane θ – 2θ and pole figure X-ray diffraction (XRD) scans. Transmission electron microscopy (TEM) samples were mechanically polished and thinned using low-energy Ar ion milling. TEM imaging was conducted using an FEI Talos 200X analytical microscope operated with an accelerating voltage of 200 kV. Energy-dispersive X-ray spectroscopy (EDS) was conducted using a Fischione ultra-high-resolution high-angle annular dark field (HAADF) detector and a super X EDS detector. Hardness and elastic modulus were calculated from nanoindentation measurements performed using a Berkovich tip on a Hysitron TI Premiere nanoindenter under displacement control. The indentation depth was less than 15% of the film thickness to prevent any substrate effects. Figure 1d depicts the test setup schematically and Figure 1e contains typical plots of the displacement vs. time for tests at various strain rates.

A modified nanoindentation methodology was implemented in this study to reliably probe film hardness at low strain rates [22]. Thermal drift provides a significant hurdle to reliable nanoindentation experiments when indenting at low strain rates ($\dot{\epsilon} < 0.05 \text{ s}^{-1}$) leading to significant scatter in both hardness and modulus measurements. Conventional nanoindentation calculates the reduced modulus (E_r) and hardness (H) using the following method:

$$h_c = h - \frac{0.75 \cdot P}{S} \quad (2)$$

$$A = m_0 h_c^2 + m_1 h_c \quad (3)$$

$$E_r = \frac{\sqrt{\pi}}{2} \frac{S}{\sqrt{A}} \quad (4)$$

$$H = \frac{P}{A} \quad (5)$$

where h_c is the contact depth, P is the normal applied load, S is the stiffness, A is the contact area, and m_0 and m_1 are constants determined through a calibration process using a known material. As thermal drift leads to an unreliable determination of the contact area, the modified method utilizes the standard nanoindentation method at high strain rates to measure E_r , and then back calculates A and H using Equation (5) and:

$$A = \frac{\pi}{4} \times \frac{S^2}{E_r^2} \quad (6)$$

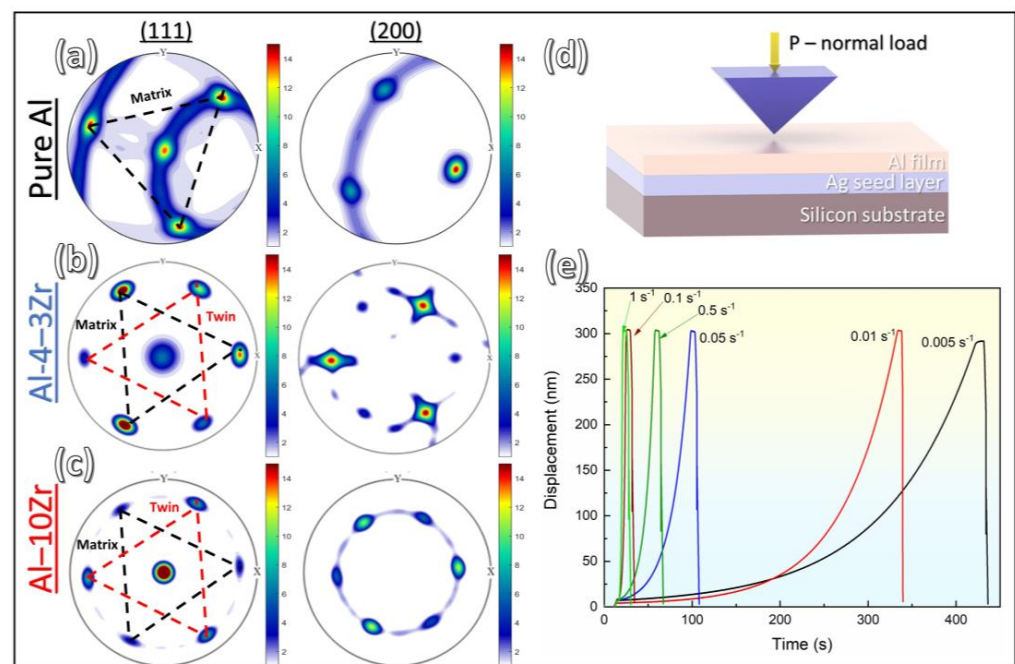


Figure 1. Comparison of (111) and (200) X-ray pole figures among (a) pure Al, (b) nanotwinned (NT) Al-4.3Zr, and (c) NT Al-10Zr, revealing strong (111) textures in all three films. The six-fold symmetry in the Al-Zr alloys indicates twin formation. (d) Schematic detailing the nanoindentation test setup used in this study. (e) Displacement vs. time plots for Al-10Zr highlighting the various constant strain rates used during each displacement-controlled nanoindentation test on each sample.

A flow chart adapted from [22] has been included as Supplementary Figure S4 to further clarify the procedure. Constant strain rate indents were performed on each sample at 6 different strain rates (0.005 s^{-1} , 0.01 s^{-1} , 0.05 s^{-1} , 0.1 s^{-1} , 0.5 s^{-1} , and 1 s^{-1}) with 75 indents performed per test to ensure statistical reliability.

3. Results

Structural and textural information for the NT Al-Zr alloys were collected using both pole figures and θ - 2θ XRD scans. Figure 1a demonstrates that the pure Al film pole figures possess three-fold symmetry, characteristic of strong (111) texture. Notably, Zr solute additions induce a shift to 6-fold symmetry in the Al-4.3Zr and Al-10Zr pole figures, indicating the formation of a high density of twin boundaries, highlighted in Figure 1b,c. The twin spot intensity is stronger in the Al-10Zr sample than the other samples, indicating that the twin density increases with higher Zr content. In the θ - 2θ XRD spectra in Supplementary Figure S1, only peaks from the Si(111) substrates and the Al films were present, suggesting no second phase formation. Peaks corresponding to the Ag (222) are present due to the seed layer.

The microstructures of the as-deposited NT Al-Zr alloys were investigated using TEM, and both plan-view (PV) and cross-section TEM (XTEM) micrographs are presented in Figure 2. Figure 2a contains a bright field (BF) PV-TEM image of the pure Al film

revealing ultra-fine grains (~ 250 nm). The selected area diffraction (SAD) patterns for pure Al (Figure 2a) and NT Al–4.3Zr (Figure 2b) identify the single-crystal-like (111) texture, which is identified by a collection of individual grains all exhibiting strong out-of-plane (111) textures. Notably, the Zr solute additions refine the microstructure down to ~ 50 nm in the NT Al–10Zr film. Figure 2c reveals a breakdown of the single-crystal-like texture and a nanocrystalline microstructure in the Al–10Zr film, as identified by the (220) diffraction ring in the corresponding SAD pattern. This textural evolution has been explored and discussed in our previous work [45,46]. The grain size distributions are presented in Supplementary Figure S2 with over 100 measurements per sample. Supplementary Figure S3 contains EDS maps collected using TEM, which reveals a complete solid solution of Zr solute into the Al matrix. XTEM images are presented in Figure 2d–f to further assess the microstructural evolution as Zr solute content increases. The pure Al film (Figure 2d) is composed of coarse columns (~ 250 nm) with no twin boundaries identified through the corresponding SAD pattern. Figure 2e,f reveal the NT Al–Zr films are composed of an abundance of vertically oriented $\Sigma 3(112)$ incoherent twin boundaries (ITBs). The twinned diffraction spots in the corresponding SAD patterns in Figure 2e,f confirm the presence of vertically oriented twin boundaries. In addition, the $\frac{1}{3}(\bar{1}\bar{1}1)$ spots present in the SAD patterns in Figure 2e,f confirm the presence of stacking faults composing diffuse ITBs or the 9R phase. The HRTEM image inset in Figure 2f depicts the periodic stacking fault array constructing the 9R phase, with the fast Fourier transform (FFT) containing both twin spots and the $\frac{1}{3}(\bar{1}\bar{1}1)$ mentioned previously. The hardness was measured using displacement-controlled nanoindentation, and the resulting hardness values are plotted with Zr content in Figure 3a.

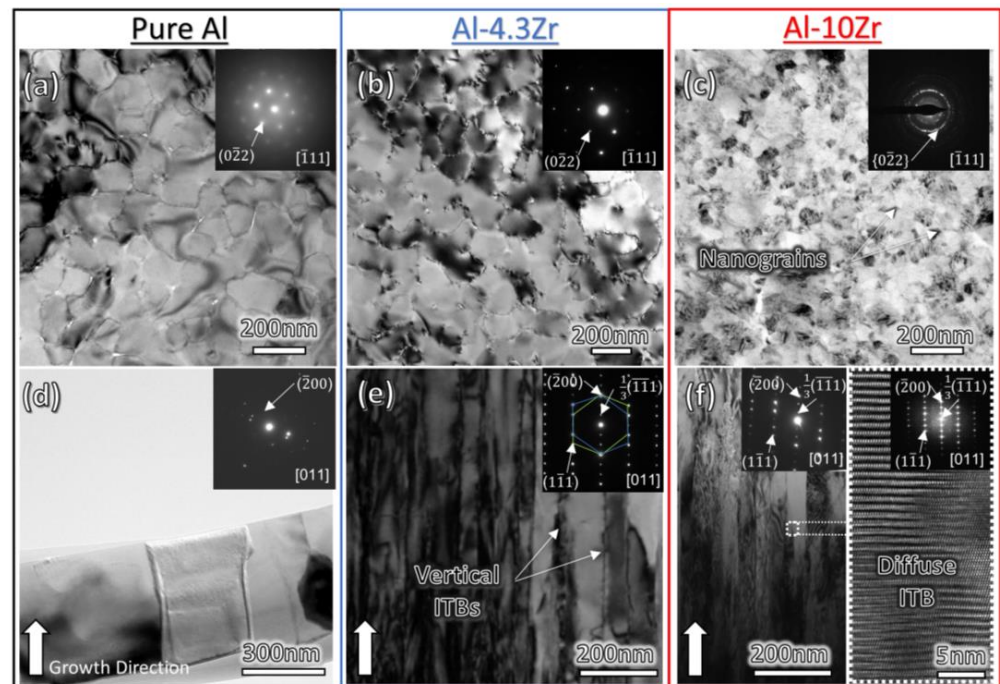


Figure 2. (a) Plan-view (PV) transmission electron microscopy (TEM) micrograph of the ultra-fine-grained pure Al film with the corresponding inserted selected area diffraction (SAD) pattern revealing the single-crystal-like (111) out-of-plane texture. (b) PV-TEM micrograph of the NT Al–4.3Zr alloy film revealing fine grains and the corresponding SAD pattern identifying the single-crystal-like (111) texture. (c) PV-TEM micrograph of the NT Al–10Zr alloy film revealing fine grains and the corresponding SAD pattern showing a strong (111) out-of-plane texture. (d) Cross-section TEM (XTEM) micrograph of pure Al with the corresponding SAD pattern. (e) XTEM micrograph of the NT Al–4.3Zr alloy with the corresponding SAD pattern revealing columnar nanotwin boundaries. (f) XTEM micrograph of the NT Al–10Zr alloy with the corresponding SAD pattern revealing columnar nanotwin boundaries and a high-resolution TEM (HRTEM) inset highlighting the periodic stacking fault array in diffuse ITBs or the 9R phase.

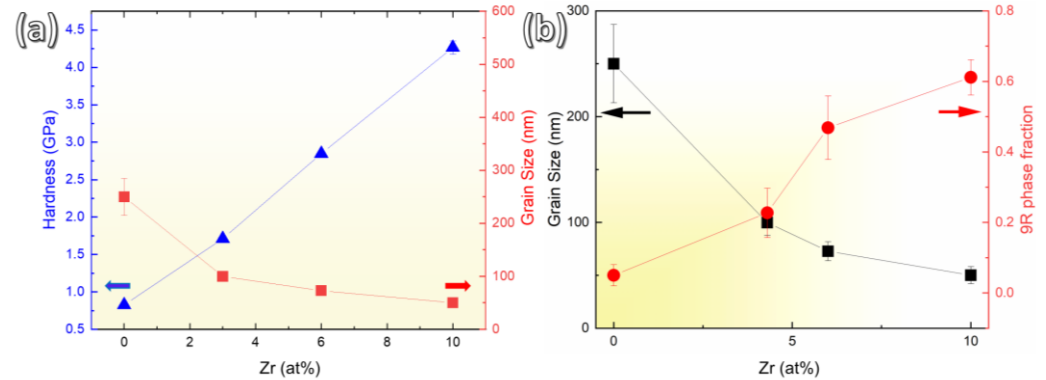


Figure 3. (a) Hardness and grain size plotted as a function of Zr solute concentration. (b) Plot detailing the evolution of grain size and 9R phase fraction with the concentration of Zr.

Figure 3b plots the grain size and 9R phase fraction against the Zr content, revealing significant grain size reduction down to ~50 nm as well as a consistent increase in the 9R fraction with increasing Zr content. The 9R phase fraction was determined using HRTEM analysis of ~100 grains per sample and the details of the calculation are provided in [45]. A monotonic increase in hardness is identified with increasing Zr content, with the NT Al–10Zr films reaching a hardness of ~4.2 GPa. Constant strain rate nanoindentation was also conducted at the six different strain rates, as presented in Figure 1e. Figure 4a compares the results from the conventional and modified nanoindentation methods [22] and demonstrates the reliability of the modified method at low strain rates. In contrast, the conventional method introduces unusually high hardness and large variations at low strain rates. As the SRS of a material is a measure of the change in flow stress for various strain rates ($m = \frac{\partial \sigma}{\partial \ln \dot{\epsilon}} = \frac{\ln \sigma}{\ln \dot{\epsilon}}$), H must be divided by the Taylor factor (~3) in order to estimate the film flow stress. Accordingly, the results from the constant strain rate tests are presented as $\ln(H/3)$ vs. $\ln(\dot{\epsilon})$ in Figure 4b, where the slope gives the SRS value, m . The pure Al films exhibit a m of ~0.0094, which corresponds well with previous studies. Notably, increasing the Zr content and twin density leads to a jump in m up to 0.0187 and 0.0297 in the NT Al–4.3Zr and Al–10Zr coatings.

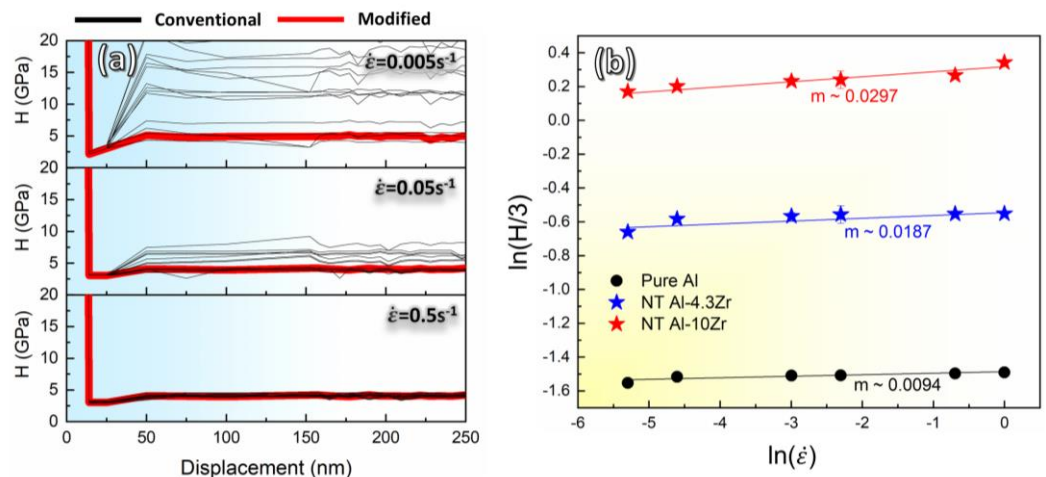


Figure 4. (a) Comparisons of hardness vs. displacement plots for the NT Al–10Zr specimen by using the conventional and modified nanoindentation method at various strain rates. (b) Comparison of constant strain rate nanoindentation results among Al, and NT Al–4.3Zr and Al–10Zr films revealing an increase in strain rate sensitivity (m) at higher Zr content.

4. Discussion

The unique NT microstructure presented in this study originates from a few factors. First, the dominant (111) texture promotes twin formation during the nucleation and growth of the sputtered Al–Zr coatings. The Zr solute improves this texture, whereas the pure Al films are polycrystalline in nature and composed of randomly oriented grains. $\Sigma 3(112)$ ITBs, shown in Figure 2e,f, form along specific crystallographic planes which are prevalent in (111)-textured films. The difference in microstructure between pure Al and NT Al–Zr is stark as the strong texture alters the grain boundary structure, promoting ITBs in NT Al. Second, the high quench rates experienced during magnetron sputtering trap a higher volume fraction of Zr solute atoms in the solution, generating a supersaturated solid solution [59]. The Zr solute facilitates significant grain refinement and a strong (111) texture, as depicted in Figure 3a, leading to an abundance of vertically oriented ITBs. The high SFE of Al and the lack of solute leads to a microstructure of randomly oriented high-angle grain boundaries in pure Al. The 9R phase is the nomenclature used to describe diffuse ITBs, and an example of this is provided in the HRTEM micrograph in Figure 2f. Based on HRTEM evidence of ITBs in pure Cu and molecular dynamics simulations, ITBs are composed of a periodic array of three Shockley partial dislocations with a $b_2:b_1:b_3$ arrangement involving three adjacent {111} planes [48,60–63]. The b_2 and b_3 Shockley partials are relatively immobile mixed dislocations with $1/6 [\bar{2}11]$ and $1/6 [1\bar{2}1]$ Burgers vectors, respectively. The b_1 Shockley partial is a pure edge dislocation with a Burgers vector of $1/6 [11\bar{2}]$. b_1 is able to glide due to a smaller Peierls barrier, leading to diffuse ITBs or the 9R phase [61]. MD simulations demonstrate the contribution of Fe solute in stabilizing the 9R phase in pure Al [48]. The high SFE of Al prevents 9R formation in pure Al, whereas the Zr solute stabilizes the diffuse ITB structure by pinning the Shockley partials. Figure 3b reflects the increase in the 9R phase identified at higher Zr solute levels.

The hardness of NT Al–Zr reaches 4.2 GPa, as shown in Figure 3a, which is high compared to classical Al alloys. The strengthening mechanisms contributing to this high hardness include solid solution strengthening and boundary strengthening. Per our previous work, the contribution from solid solution strengthening was calculated based on the Fleischer formulation [45]. Despite the supersaturated solid solution stabilized by the high sputter quench rate, it was found that solid solution strengthening only contributes ~28 MPa in the Al–10Zr alloy. This value is far below the measured hardness, and since the XRD spectra presented in Supplementary Figure S1 identify no second phase formation, boundary strengthening was determined to be the main factor behind the improved mechanical properties. The Hall–Petch coefficient for NT Al–Zr alloys was determined to be ~9.3 GPa·nm^{1/2}, which is almost twice that for nanocrystalline Al [45,46]. As MD simulations and in situ nanoindentation experiments demonstrate that ITBs obstruct dislocation motion and transmission similar to conventional grain boundaries [64], the jump in the Hall–Petch slope can be attributed to the high density of stacking faults composing the 9R phase. Our previous work determined that the 9R phase contributes ~6.9 GPa·nm^{1/2} to the Hall–Petch slope, supporting the significant role stacking faults can play in mechanical properties. This analysis corresponds well with previous MD simulations identifying extensive interactions between dislocations and the 9R phase in NT Al–Fe [48]. Su et al. also demonstrated an enhancement of mechanical properties in Co thin films with an abundance of stacking faults [65].

The modified nanoindentation method implemented in this study enabled the probing of the strain rate sensitivity of NT Al–Zr alloys. To minimize data skew at low strain rates due to thermal drift, the modified method from Liu et al. [22] was utilized to analyze the constant strain rate nanoindentation data. The indented area at low strain rates (A) was calculated based on the reduced elastic modulus (E_r) measured at high strain rates, mitigating the issue of thermal drift at low strain rates. This approach enables quick analysis of the already collected data while maintaining consistency across the test methods at different strain rates. Figure 4a compares the hardness values as a function of indentation depth and underscores the issues with the conventional method at low strain rates. High

levels of thermal drift at low strain rates (0.005 s^{-1}) induce artificially high hardness and large skew in the data compared with the high strain rates (0.5 s^{-1}). Figure 4a highlights the consistency and reliability of the modified method as the data are consistent and reproducible. To assess the performance of these coatings and to further validate the results from this study, we compared the m values collected in this work with prior studies on various FCC metals (Figure 5a) implementing various test techniques (tensile testing, compression, and rate jump tests) in Figure 5a [23,66–73]. It has been well documented that m increases with decreasing grain size in FCC metal systems, and Figure 5b reflects the same trend [24]. The pure Al film exhibits a similar rate sensitivity ($m = 0.0094$) as the ultra-fine-grained Al and Cu tested using bulk methods, which further validates the methodology used in this work. Compared with bulk Al and Al alloys, the NT Al–4.3Zr and Al–10Zr alloys have greater m values [69], increasing to 0.0297 in the Al–10Zr alloy. This finding suggests the presence of ITBs and 9R phase bolster the SRS in NT Al alloys.

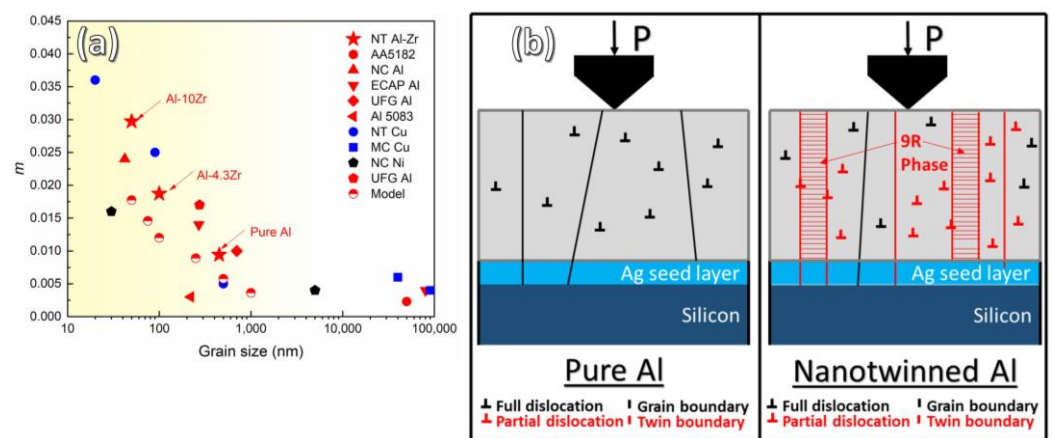


Figure 5. (a) Comparison of known values of m for various FCC metals (Al, Ni, and Cu) plotted as a function of grain size as tested using various techniques. The results from the nanoindentation technique are consistent with previous findings and highlight the bolstered strain rate sensitivity in NT Al–Zr alloys [22,24,58,66–71]. (b) Schematic comparing the UFG Al film with full dislocations and conventional grain boundaries (GBs) with the NT Al–Zr alloys composed of a mixture of GBs and ITBs as well as an abundance of partial dislocations (9R phase).

The SRS of NC FCC metals has been shown to be highly dependent on grain size (d) [24–26], and is given by [74]:

$$m = \frac{kT}{\zeta b} \cdot \frac{1}{\chi(\alpha\mu b\sqrt{\rho}d) + \beta\sqrt{d}} \quad (7)$$

where k is Boltzmann’s constant, b is the Burgers vector, μ is the shear modulus, ζ is the distance swept by a glide dislocation, and α , β , and χ are proportional factors. This model suggests that m will increase as grain size decreases, in agreement with the results from this study [74,75]. Equation (7) provides insight into the grain-size-dependent variation of m . However, its application to specific cases is difficult as it depends on a number of proportional factors that are yet to be determined [74]. The estimated m for NC Al with a grain size of 50 nm is 0.017, which is below that of NT Al–10Zr with a similar grain size. This difference can be attributed to multiple factors that are accounted for within the model itself, including the magnitude of b , the dislocation density (ρ) providing dislocation barriers during deformation, and the activation volume, represented by ζ . The influence of grain size has been isolated as a factor as the plots in Figure 5a directly compare m in NT Al–Zr with various FCC metals composed of similar grain sizes (columnar twin spacing in this study). First, as demonstrated in the HRTEM micrograph in Figure 2f and depicted schematically in Figure 5c, introducing an abundance of ITBs provides a high

density of mobile Shockley partial dislocations that carry plasticity. The b of these partial dislocations is $\frac{1}{6}\langle 112 \rangle$, which is smaller in magnitude than the full dislocations operating in NC Al at similar grain sizes (60–100 nm). As captured in Equation (2), dislocations with a smaller b will increase m . Incorporating this factor into the model increases the predicted m from 0.017 to 0.033, which is closer to the experimentally measured m of 0.0294. Second, ρ increases slightly due to the presence of partial dislocations composing the 9R phase. However, the current model accounts for a moderate pre-existing dislocation density and any slight changes are muted by the inverse square root relationship between ρ and m . Finally, ζ is expected to decrease in NT Al alloys since the high-density stacking faults composing the 9R phase provide additional barriers to dislocation motion, leading to an increase in m .

Previous research exploring the SRS of NT Cu has highlighted the role that coherent twin boundaries (CTBs) play in improving mechanical properties [28,29]. Refining twin spacing to ~15 nm bolstered strength to 900 MPa while maintaining significant plasticity [29]. The concomitant high strength and ductility are attributed to an abundance of pre-existing mobile partial dislocations forming steps on the CTBs, the density of which increases at finer twin thicknesses [29]. Similarly, Lu et al. investigated the influence of these nanoscale twins on rate sensitivity and found that increasing twin density improved m [71]. The increased m values were attributed to extensive dislocation interactions with CTBs and an increased dislocation generation from the steps along CTBs. In situ nanoindentation tests of CTBs in Cu revealed that Shockley partial dislocations can propagate along CTBs, promoting extensive dislocation activity within twins [76,77]. As the 9R phase identified in NT Al–Zr is composed of arrays of mobile Shockley partial dislocations, it is likely responsible for the improved SRS of NT Al–Zr [45,61]. Although the high strength and deformability of NT Al alloys has been extensively documented through in situ micropillar compression [44,46,53,78,79], there have been no attempts to characterize the SRS of this unique microstructure composed of vertically aligned ITBs. Figure 5b contrasts the pure Al and NT Al–Zr microstructures. Plasticity in the pure Al films is dominated by full-dislocation motion since the grain size is on the order of a few hundred nanometers, and the SRS follows previous model predictions in the literature. In comparison, Figure 5b depicts the increase in partial dislocations in NT Al alloys accompanying the increased twin density, and the mobility of these partials drives the boost in SRS. Accompanying the boost in plasticity, the abundance of 9R phase and Shockley partials captured in the HRTEM in Figure 2f provides a source for improving m . As mentioned previously, the decrease in b provides another source for the rate sensitivity increase in NT Al–Zr. Ultimately, the microstructural complexity of NT Al–Zr is crucial in maintaining high strength and plasticity [46,48], and its influence on SRS is evidenced through this study.

5. Conclusions

The application of a constant strain rate nanoindentation methodology enabled the probing of strain rate sensitivity of NT Al–Zr sputtered films. Increasing Zr content leads to significant grain refinement down to 50 nm, and the promotion of incoherent twin boundaries and the 9R phase led to a corresponding jump in hardness up to 4.2 GPa. Similarly, increasing the Zr content also boosts strain rate sensitivity in NT Al–Zr alloys, which has been linked to the increase in partial dislocation density and mobility. This study represents a major finding and fills a previously unexplored gap in the literature and identifies the role incoherent twin boundaries play in improving the strain rate sensitivity, and ultimately the deformability and fracture resistance, of NT Al–Zr alloys.

Supplementary Materials: The following supporting information can be downloaded at: <https://www.mdpi.com/article/10.3390/cryst13020276/s1>, Figure S1. XRD spectra revealing strong (111) texture in as-deposited films (Pure Al, Al-4.3Zr and Al-10Zr). Figure S2. Histograms showing grain size distribution for Pure Al, Al-4.3Zr and Al-10Zr. Figure S3. EDS maps of (a) Al-4.3Zr and (b) Al-10Zr demonstrating obvious solid solution and no segregation or phase separation. Figure S4. Flow

chart detailing the differences between conventional and the modified nanoindentation method for measuring hardness at low strain rates.

Author Contributions: Conceptualization, N.A.R. and X.Z.; Methodology, N.A.R.; Validation, N.A.R., B.Y., and B.T.S.; Formal Analysis, N.A.R.; Investigation, N.A.R. and X.S.; Resources, N.A.R.; Data Curation, N.A.R.; Writing—original draft, N.A.R.; Writing—review and editing, N.A.R. and X.Z.; Visualization, N.A.R.; Supervision, X.Z.; Project administration, H.W. and X.Z.; Funding acquisition, N.A.R. All authors have read and agreed to the published version of the manuscript.

Funding: This project is primarily funded by DoE-BES (Basic Energy Sciences) under grant no. DE-SC0016337. The ASTAR crystal orientation system in the TEM microscope is supported by ONR-DURIP award N00014-17-1-2921. Access to the Microscopy Facilities at Purdue University and the Center for Integrated Nanotechnologies (managed by Los Alamos National Laboratory) is also acknowledged.

Data Availability Statement: Data are available upon request.

Conflicts of Interest: The authors declare no conflict of interest.

References

1. Hansen, N. Hall-Petch Relation and Boundary Strengthening. *Scr. Mater.* **2004**, *51*, 801–806. [[CrossRef](#)]
2. Petch, N.J. The Cleavage Strength of Polycrystals. *J. Iron Steel Inst.* **1953**, *174*, 25–28.
3. Hall, E.O. The Deformation and Ageing of Mild Steel: III Discussion and Results. *Proc. Phys. Soc. Sect. B* **1951**, *64*, 747–753. [[CrossRef](#)]
4. Yang, B.; Shang, Z.; Ding, J.; Lopez, J.; Jarosinski, W.; Sun, T.; Richter, N.; Zhang, Y.; Wang, H.; Zhang, X. Investigation of Strengthening Mechanisms in an Additively Manufactured Haynes 230 Alloy. *Acta Mater.* **2022**, *222*, 117404. [[CrossRef](#)]
5. Gleiter, H. Nanostructured Materials: Basic Concepts and Microstructure. *Acta Mater.* **2000**, *48*, 1–29. [[CrossRef](#)]
6. Kumar, K.S.; Van Swygenhoven, H.; Suresh, S. Mechanical Behavior of Nanocrystalline Metals and Alloys. *Acta Mater.* **2003**, *51*, 5743–5774. [[CrossRef](#)]
7. Ding, J.; Xue, S.; Shang, Z.; Li, J.; Zhang, Y.; Su, R.; Niu, T.; Wang, H.; Zhang, X. Characterization of Precipitation in Gradient Inconel 718 Superalloy. *Mater. Sci. Eng. A* **2021**, *804*, 140718. [[CrossRef](#)]
8. Sun, T.; Shang, Z.; Cho, J.; Ding, J.; Niu, T.; Zhang, Y.; Yang, B.; Xie, D.; Wang, J.; et al. Ultra-Fine-Grained and Gradient FeCrAl Alloys with Outstanding Work Hardening Capability. *Acta Mater.* **2021**, *215*, 117049. [[CrossRef](#)]
9. Sergueeva, A.V.; Song, C.; Valiev, R.Z.; Mukherjee, A.K. Structure and Properties of Amorphous and Nanocrystalline NiTi Prepared by Severe Plastic Deformation and Annealing. *Mater. Sci. Eng. A* **2003**, *339*, 159–165. [[CrossRef](#)]
10. Liao, X.Z.; Zhao, Y.H.; Srinivasan, S.G.; Zhu, Y.T.; Valiev, R.Z.; Gunderov, D.V. Deformation Twinning in Nanocrystalline Copper at Room Temperature and Low Strain Rate. *Appl. Phys. Lett.* **2004**, *84*, 592–594. [[CrossRef](#)]
11. Pinto, E.M.; Ramos, A.S.; Vieira, M.T.; Brett, C.M.A. A Corrosion Study of Nanocrystalline Copper Thin Films. *Corros. Sci.* **2010**, *52*, 3891–3895. [[CrossRef](#)]
12. Simoes, S.; Calinas, R.; Vieira, M.T.F.; Ferreira, P.J. In Situ TEM Study of Grain Growth in Nanocrystalline Copper Thin Films. *Nanotechnology* **2010**, *21*, 145701. [[CrossRef](#)]
13. Gai, P.L.; Mitra, R.; Weertman, J.R. Structural Variations in Nanocrystalline Nickel Films. *Pure Appl. Chem.* **2002**, *74*, 1519–1526. [[CrossRef](#)]
14. Li, Q.; Shang, Z.; Sun, X.; Fan, C.; Su, R.; Richter, N.A.; Fan, Z.; Zhang, Y.; Xue, S.; Wang, H.; et al. High-Strength and Tunable Plasticity in Sputtered Al–Cr Alloys with Multistage Phase Transformations. *Int. J. Plast.* **2021**, *137*, 102915. [[CrossRef](#)]
15. Niu, T.; Zhang, Y.; He, Z.; Sun, T.; Richter, N.A.; Wang, H.; Zhang, X. Texture Development in Cu–Ag–Fe Triphase Immiscible Nanocomposites with Superior Thermal Stability. *Acta Mater.* **2023**, *244*, 118545. [[CrossRef](#)]
16. Ganapathi, S.K.; Aindow, M.; Fraser, H.L.; Rigney, D.A. A Comparative Study of the Nanocrystalline Material Produced by Sliding Wear and Inert Gas Condensation. *Mater. Res. Soc. Symp. Proc.* **1991**, *206*, 593–598. [[CrossRef](#)]
17. Nieman, G.W.; Weertman, J.R.; Siegel, R.W. Microhardness of Nanocrystalline Palladium and Copper Produced by Inert-Gas Condensation. *Scr. Metall.* **1989**, *23*, 2013–2018. [[CrossRef](#)]
18. Wu, X.J.; Du, L.G.; Zhang, H.F.; Liu, J.F.; Zhou, Y.S.; Li, Z.Q.; Xiong, L.Y.; Bai, Y.L. Synthesis and Tensile Property of Nanocrystalline Metal Copper. *Nanostructured Mater.* **1999**, *12*, 221–224. [[CrossRef](#)]
19. Wang, J.; Wu, S.; Fu, S.; Liu, S.; Yan, M.; Lai, Q.; Lan, S.; Hahn, H.; Feng, T. Ultrahigh Hardness with Exceptional Thermal Stability of a Nanocrystalline CoCrFeNiMn High-Entropy Alloy Prepared by Inert Gas Condensation. *Scr. Mater.* **2020**, *187*, 335–339. [[CrossRef](#)]
20. Hull, R.; Gibson, J.M.; Brus, L.E.; Norris, D.J.; Bawendi, M.G.; Zunger, A.; Zunger, A.; Whaley, K.B.; Williamson, A.J.; Reboledo, F.A.; et al. Grain Boundary–Mediated Plasticity in Nanocrystalline Nickel. *Science* **2004**, *305*, 654–658.
21. Liang, R.; Khan, A.S. A Critical Review of Experimental Results and Constitutive Models for BCC and FCC Metals over a Wide Range of Strain Rates and Temperatures. *Int. J. Plast.* **1999**, *15*, 963–980. [[CrossRef](#)]

22. Liu, Y.; Hay, J.; Wang, H.; Zhang, X. A New Method for Reliable Determination of Strain-Rate Sensitivity of Low-Dimensional Metallic Materials by Using Nanoindentation. *Scr. Mater.* **2014**, *77*, 5–8. [[CrossRef](#)]
23. Hayes, R.W.; Witkin, D.; Zhou, F.; Lavernia, E.J. Deformation and Activation Volumes of Cryomilled Ultrafine-Grained Aluminum. *Acta Mater.* **2004**, *52*, 4259–4271. [[CrossRef](#)]
24. Chen, J.; Lu, L.; Lu, K. Hardness and Strain Rate Sensitivity of Nanocrystalline Cu. *Scr. Mater.* **2006**, *54*, 1913–1918. [[CrossRef](#)]
25. Wei, Q.; Cheng, S.; Ramesh, K.T.; Ma, E. Effect of Nanocrystalline and Ultrafine Grain Sizes on the Strain Rate Sensitivity and Activation Volume: Fcc versus Bcc Metals. *Mater. Sci. Eng. A* **2004**, *381*, 71–79. [[CrossRef](#)]
26. Wei, Y.; Bower, A.F.; Gao, H. Enhanced Strain-Rate Sensitivity in Fcc Nanocrystals Due to Grain-Boundary Diffusion and Sliding. *Acta Mater.* **2008**, *56*, 1741–1752. [[CrossRef](#)]
27. Malygin, G.A. Analysis of the Strain-Rate Sensitivity of Flow Stresses in Nanocrystalline FCC and BCC Metals. *Phys. Solid State* **2007**, *49*, 2266–2273. [[CrossRef](#)]
28. Lu, L.; Shen, Y.; Chen, X.; Qian, L.; Lu, K. Ultrahigh Strength and High Electrical Conductivity in Copper. *Science* **2004**, *304*, 422–426. [[CrossRef](#)]
29. Lu, L.; Chen, X.; Huang, X.; Lu, K. Revealing the Maximum Strength in Nanotwinned Copper. *Science* **2009**, *323*, 607–610. [[CrossRef](#)]
30. Fang, Q.; Sansoz, F. Columnar Grain-Driven Plasticity and Cracking in Nanotwinned FCC Metals. *Acta Mater.* **2021**, *212*, 116925. [[CrossRef](#)]
31. Anderoglu, O.; Misra, A.; Wang, H.; Ronning, F.; Hundley, M.F.; Zhang, X. Epitaxial Nanotwinned Cu Films with High Strength and High Conductivity. *Appl. Phys. Lett.* **2008**, *93*, 5–8. [[CrossRef](#)]
32. Zhang, X.; Anderoglu, O.; Misra, A.; Wang, H. Influence of Deposition Rate on the Formation of Growth Twins in Sputter-Deposited 330 Austenitic Stainless Steel Films. *Appl. Phys. Lett.* **2007**, *90*, 2007–2009. [[CrossRef](#)]
33. Yu, K.Y.; Bufford, D.; Chen, Y.; Liu, Y.; Wang, H.; Zhang, X. Basic Criteria for Formation of Growth Twins in High Stacking Fault Energy Metals. *Appl. Phys. Lett.* **2013**, *103*, 181903. [[CrossRef](#)]
34. Zhang, Y.F.; Su, R.; Niu, T.J.; Richter, N.A.; Xue, S.; Li, Q.; Ding, J.; Yang, B.; Wang, H.; Zhang, X. Thermal Stability and Deformability of Annealed Nanotwinned Al/Ti Multilayers. *Scr. Mater.* **2020**, *186*, 219–224. [[CrossRef](#)]
35. Zhang, Y.F.; Li, Q.; Gong, M.; Xue, S.; Ding, J.; Li, J.; Cho, J.; Niu, T.; Su, R.; Richter, N.A.; et al. Deformation Behavior and Phase Transformation of Nanotwinned Al/Ti Multilayers. *Appl. Surf. Sci.* **2020**, *527*, 146776. [[CrossRef](#)]
36. Xiao, J.; Deng, C. Mitigating the Hall-Petch Breakdown in Nanotwinned Cu by Amorphous Intergranular Films. *Scr. Mater.* **2021**, *194*, 113682. [[CrossRef](#)]
37. Stobbs, W.M.; Sworn, C.H. The Weak Beam Technique as Applied to the Determination of the Stacking-Fault Energy of Copper. *Philos. Mag.* **1971**, *24*, 1365–1381. [[CrossRef](#)]
38. Bufford, D.; Wang, H.; Zhang, X. High Strength, Epitaxial Nanotwinned Ag Films. *Acta Mater.* **2011**, *59*, 93–101. [[CrossRef](#)]
39. Howie, A.; Swann, P.R. Direct Measurements of Stacking-Fault Energies from Observations of Dislocation Nodes. *Philos. Mag.* **1961**, *6*, 1215–1226. [[CrossRef](#)]
40. Vitos, L.; Nilsson, J.O.; Johansson, B. Alloying Effects on the Stacking Fault Energy in Austenitic Stainless Steels from First-Principles Theory. *Acta Mater.* **2006**, *54*, 3821–3826. [[CrossRef](#)]
41. Frøseth, A.G.; Derlet, P.M.; Van Swygenhoven, H. Twinning in Nanocrystalline Fcc Metals. *Adv. Eng. Mater.* **2005**, *7*, 16–20. [[CrossRef](#)]
42. Xue, S.; Kuo, W.; Li, Q.; Fan, Z.; Ding, J.; Su, R.; Wang, H.; Zhang, X. Texture-Directed Twin Formation Propensity in Al with High Stacking Fault Energy. *Acta Mater.* **2018**, *144*, 226–234. [[CrossRef](#)]
43. Xue, S.; Fan, Z.; Chen, Y.; Li, J.; Wang, H.; Zhang, X. The Formation Mechanisms of Growth Twins in Polycrystalline Al with High Stacking Fault Energy. *Acta Mater.* **2015**, *101*, 62–70. [[CrossRef](#)]
44. Richter, N.A.; Zhang, Y.F.; Gong, M.; Niu, T.; Yang, B.; Xue, S.; Wang, J.; Wang, H.; Zhang, X. Solute Synergy Induced Thermal Stability of High-Strength Nanotwinned Al-Co-Zr Alloys. *Mater. Sci. Eng. A* **2023**, *862*, 144477. [[CrossRef](#)]
45. Richter, N.A.; Zhang, Y.F.; Xie, D.Y.; Su, R.; Li, Q.; Xue, S.; Niu, T.; Wang, J.; Wang, H.; Zhang, X.; et al. Microstructural Evolution of Nanotwinned Al-Zr Alloy with Significant 9R Phase. *Mater. Res. Lett.* **2020**, *9*, 91–98. [[CrossRef](#)]
46. Richter, N.A.; Gong, M.; Zhang, Y.F.; Niu, T.; Yang, B.; Wang, J.; Wang, H.; Zhang, X. Exploring the Deformation Behavior of Nanotwinned Al-Zr Alloy via in Situ Compression. *J. Appl. Phys.* **2022**, *132*, 065104. [[CrossRef](#)]
47. Gong, M.; Wu, W.; Xie, D.; Richter, N.A.; Li, Q.; Zhang, Y.; Xue, S.; Zhang, X.; Wang, J.; Gong, M.; et al. First-Principles Calculations for Understanding Microstructures and Mechanical Properties of Co-Sputtered Al Alloys. *Nanoscale* **2021**, *13*, 14987–15001. [[CrossRef](#)]
48. Li, Q.; Xue, S.; Wang, J.; Shao, S.; Kwong, A.H.; Giwa, A.; Fan, Z.; Liu, Y.; Qi, Z.; Ding, J.; et al. High-Strength Nanotwinned Al Alloys with 9R Phase. *Adv. Mater.* **2018**, *30*, 1704629. [[CrossRef](#)]
49. Zhang, Y.F.; Xue, S.; Li, Q.; Fan, C.; Su, R.; Ding, J.; Wang, H.; Wang, H.; Zhang, X. Microstructure and Mechanical Behavior of Nanotwinned AlTi Alloys with 9R Phase. *Scr. Mater.* **2018**, *148*, 5–9. [[CrossRef](#)]
50. Zhang, Y.; Niu, T.; Richter, N.A.; Sun, T.; Li, N.; Wang, H.; Zhang, X. Tribological Behaviors of Nanotwinned Al Alloys. *Appl. Surf. Sci.* **2022**, *600*, 154108. [[CrossRef](#)]
51. Li, Q.; Xue, S.; Fan, C.; Richter, N.A.; Zhang, Y.; Chen, Y.; Wang, H.; Zhang, X. Epitaxial Nanotwinned Metals and Alloys: Synthesis-Twin Structure-Property Relations. *CrystEngComm* **2021**, *23*, 6637–6649. [[CrossRef](#)]
52. Zhang, Y.F.; Li, Q.; Xue, S.C.; Ding, J.; Xie, D.Y.; Li, J.; Niu, T.; Wang, H.; Wang, H.; Wang, J.; et al. Ultra-Strong Nanotwinned Al-Ni Solid Solution Alloys with Significant Plasticity. *Nanoscale* **2018**, *10*, 22025–22034. [[CrossRef](#)]

53. Zhang, Y.F.; Su, R.; Xie, D.Y.; Niu, T.J.; Xue, S.; Li, Q.; Shang, Z.; Ding, J.; Richter, N.A.; Wang, J.; et al. Design of Super-Strong and Thermally Stable Nanotwinned Al Alloys: Via Solute Synergy. *Nanoscale* **2020**, *12*, 20491–20505. [[CrossRef](#)] [[PubMed](#)]
54. Bayoumy, D.; Schliephake, D.; Dietrich, S.; Wu, X.H.; Zhu, Y.M.; Huang, A.J. Intensive Processing Optimization for Achieving Strong and Ductile Al-Mn-Mg-Sc-Zr Alloy Produced by Selective Laser Melting. *Mater. Des.* **2021**, *198*, 109317. [[CrossRef](#)]
55. Wang, Z.; Lin, X.; Kang, N.; Chen, J.; Tang, Y.; Tan, H.; Yu, X.; Yang, H.; Huang, W. Directed Energy Deposition Additive Manufacturing of a Sc/Zr-Modified Al-Mg Alloy: Effect of Thermal History on Microstructural Evolution and Mechanical Properties. *Mater. Sci. Eng. A* **2021**, *802*, 140606. [[CrossRef](#)]
56. Ma, R.; Peng, C.; Cai, Z.; Wang, R.; Zhou, Z.; Li, X.; Cao, X. Manipulating the Microstructure and Tensile Properties of Selective Laser Melted Al-Mg-Sc-Zr Alloy through Heat Treatment. *J. Alloy. Compd.* **2020**, *831*, 154773. [[CrossRef](#)]
57. Dao, M.; Lu, L.; Shen, Y.F.; Suresh, S. Strength, Strain-Rate Sensitivity and Ductility of Copper with Nanoscale Twins. *Acta Mater.* **2006**, *54*, 5421–5432. [[CrossRef](#)]
58. Choi, I.C.; Kim, Y.J.; Wang, Y.M.; Ramamurty, U.; Jang, J.-I. Nanoindentation Behavior of Nanotwinned Cu: Influence of Indenter Angle on Hardness, Strain Rate Sensitivity and Activation Volume. *Acta Mater.* **2013**, *61*, 7313–7323. [[CrossRef](#)]
59. Chu, J.P.; Lai, Y.W.; Lin, T.N.; Wang, S.F. Deposition and Characterization of TiNi-Base Thin Films by Sputtering. *Mater. Sci. Eng. A* **2000**, *277*, 11–17. [[CrossRef](#)]
60. Wang, J.; Li, N.; Anderoglu, O.; Zhang, X.; Misra, A.; Huang, J.Y.; Hirth, J.P. Detwinning Mechanisms for Growth Twins in Face-Centered Cubic Metals. *Acta Mater.* **2010**, *58*, 2262–2270. [[CrossRef](#)]
61. Wang, J.; Anderoglu, O.; Hirth, J.P.; Misra, A.; Zhang, X. Dislocation Structures of $\Sigma 3$ {112} Twin Boundaries in Face Centered Cubic Metals. *Appl. Phys. Lett.* **2009**, *95*, 93–96. [[CrossRef](#)]
62. Li, N.; Wang, J.; Zhang, X.; Misra, A. In-Situ TEM Study of Dislocation-Twin Boundaries Interaction in Nanotwinned Cu Films. *Jom* **2011**, *63*, 62. [[CrossRef](#)]
63. Bufford, D.; Bi, Z.; Jia, Q.X.; Wang, H.; Zhang, X. Nanotwins and Stacking Faults in High-Strength Epitaxial Ag/Al Multilayer Films. *Appl. Phys. Lett.* **2012**, *101*, 223112. [[CrossRef](#)]
64. Bufford, D.; Liu, Y.; Wang, J.; Wang, H.; Zhang, X. In Situ Nanoindentation Study on Plasticity and Work Hardening in Aluminium with Incoherent Twin Boundaries. *Nat. Commun.* **2014**, *5*, 4864. [[CrossRef](#)]
65. Su, R.; Neffati, D.; Xue, S.; Li, Q.; Fan, Z.; Liu, Y.; Wang, H.; Kulkarni, Y.; Zhang, X. Deformation Mechanisms in FCC Co Dominated by High-Density Stacking Faults. *Mater. Sci. Eng. A* **2018**, *736*, 12–21. [[CrossRef](#)]
66. Follansbee, P.S.; Kocks, U.F. A Constitutive Description of the Deformation of Copper Based on the Use of the Mechanical Threshold Stress as an Internal State Variable. *Acta Metall.* **1988**, *36*, 81–93. [[CrossRef](#)]
67. Picu, R.C.; Vincze, G.; Ozturk, F.; Gracio, J.J.; Barlat, F.; Maniatty, A.M. Strain Rate Sensitivity of the Commercial Aluminum Alloy AA5182-O. *Mater. Sci. Eng. A* **2005**, *390*, 334–343. [[CrossRef](#)]
68. May, J.; Höppel, H.W.; Göken, M. Strain Rate Sensitivity of Ultrafine-Grained Aluminium Processed by Severe Plastic Deformation. *Scr. Mater.* **2005**, *53*, 189–194. [[CrossRef](#)]
69. Varam, S.; Rajulapati, K.V.; Bhanu Sankara Rao, K. Strain Rate Sensitivity Studies on Bulk Nanocrystalline Aluminium by Nanoindentation. *J. Alloy. Compd.* **2014**, *585*, 795–799. [[CrossRef](#)]
70. Dalla Torre, F.; Van Swygenhoven, H.; Victoria, M. Nanocrystalline Electrodeposited Ni: Microstructure and Tensile Properties. *Acta Mater.* **2002**, *50*, 3957–3970. [[CrossRef](#)]
71. Lu, L.; Schwaiger, R.; Shan, Z.W.; Dao, M.; Lu, K.; Suresh, S. Nano-Sized Twins Induce High Rate Sensitivity of Flow Stress in Pure Copper. *Acta Mater.* **2005**, *53*, 2169–2179. [[CrossRef](#)]
72. Izadi, E.; Rajagopalan, J. Texture Dependent Strain Rate Sensitivity of Ultrafine-Grained Aluminum Films. *Scr. Mater.* **2016**, *114*, 65–69. [[CrossRef](#)]
73. Miyamoto, H.; Ota, K.; Mimaki, T. Viscous Nature of Deformation of Ultra-Fine Grain Aluminum Processed by Equal-Channel Angular Pressing. *Scr. Mater.* **2006**, *54*, 1721–1725. [[CrossRef](#)]
74. Wei, Q. Strain Rate Effects in the Ultrafine Grain and Nanocrystalline Regimes-Influence on Some Constitutive Responses. *J. Mater. Sci.* **2007**, *42*, 1709–1727. [[CrossRef](#)]
75. Bailey, J.E.; Hirsch, P.B. The Dislocation Distribution, Flow Stress, and Stored Energy in Cold-Worked Polycrystalline Silver. *Philos. Mag.* **1960**, *5*, 485–497. [[CrossRef](#)]
76. Li, N.; Wang, J.; Misra, A.; Zhang, X.; Huang, J.Y.; Hirth, J.P. Twinning Dislocation Multiplication at a Coherent Twin Boundary. *Acta Mater.* **2011**, *59*, 5989–5996. [[CrossRef](#)]
77. Li, N.; Wang, J.; Huang, J.Y.; Misra, A.; Zhang, X. Influence of Slip Transmission on the Migration of Incoherent Twin Boundaries in Epitaxial Nanotwinned Cu. *Scr. Mater.* **2011**, *64*, 149–152. [[CrossRef](#)]
78. Li, Q.; Xie, D.; Shang, Z.; Sun, X.; Cho, J.; Zhang, Y.; Xue, S.; Wang, H.; Wang, J.; Zhang, X. Coupled Solute Effects Enable Anomalous High-Temperature Strength and Stability in Nanotwinned Al Alloys. *Acta Mater.* **2020**, *200*, 378–388. [[CrossRef](#)]
79. Li, Q.; Xue, S.; Zhang, Y.; Sun, X.; Wang, H.; Zhang, X. Plastic Anisotropy and Tension-Compression Asymmetry in Nanotwinned Al-Fe Alloys: An in-Situ Micromechanical Investigation. *Int. J. Plast.* **2020**, *132*, 102760. [[CrossRef](#)]

Disclaimer/Publisher's Note: The statements, opinions and data contained in all publications are solely those of the individual author(s) and contributor(s) and not of MDPI and/or the editor(s). MDPI and/or the editor(s) disclaim responsibility for any injury to people or property resulting from any ideas, methods, instructions or products referred to in the content.